



Experimental study on hypersonic shock–body interaction between bodies in close proximity using translucent fast pressure- and temperature-sensitive paints

Di Peng¹ · Futian Xie² · Xu Liu¹ · Jingzhou Lin² · Yongzeng Li¹ · Jun Zhong² · Qinghu Zhang² · Yingzheng Liu¹

Received: 9 October 2019 / Revised: 4 February 2020 / Accepted: 31 March 2020 / Published online: 23 April 2020
© Springer-Verlag GmbH Germany, part of Springer Nature 2020

Abstract

This work presents a successful implementation of fast-responding pressure- and temperature-sensitive paints for study of hypersonic shock–body interaction between stage separation bodies. Fast PSP and TSP were applied symmetrically on two adjacent surfaces with a minimum separation of 5 mm, and the time-resolved pressure and temperature fields were obtained in a $Ma = 6$ flow using the intensity-based approach. The technical barrier of limited optical access was overcome through the development of translucent paints that allowed back-illumination and imaging through a glass wall. The in situ calibration was generally sufficient to remove the temperature-induced error for cases with weak/mild shock impingement on the surface. For cases with strong shock impingement and large temperature gradient, temperature correction was applied on the PSP data based on the TSP results prior to the in situ calibration. The PSP results with temperature correction showed good agreement with the transducer data. The complex flow structures due to shock–body interaction were clearly visualized by PSP and TSP, which allowed detailed analysis on the effects of separation distance and inclined angle.

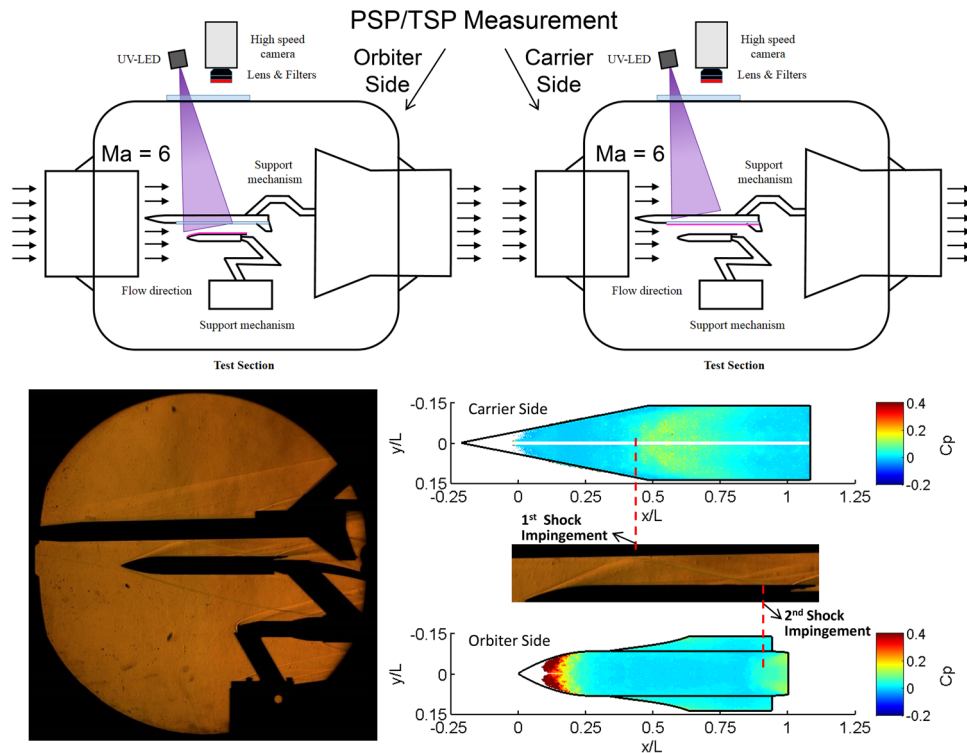
✉ Jingzhou Lin
jzou2000@sina.com

✉ Yingzheng Liu
yzliu@sjtu.edu.cn

¹ Gas Turbine Research Institute/School of Mechanical Engineering, Shanghai Jiao Tong University, 800 Dongchuan Rd., Shanghai 200240, China

² Hypervelocity Aerodynamics Institute, China Aerodynamics Research and Development Center, Mianyang 621000, China

Graphic abstract



List of symbols

C_p	Time-averaged pressure coefficient
$C_{p_{\text{pstd}}}$	Root-mean-square of time-resolved pressure coefficient
f	Frequency (Hz)
h	Vertical separation distance between the carrier and the orbiter (mm)
I	Intensity (count)
I_{PSP}	Intensity of PSP (count)
$I_{\text{PSP}_{\text{ref}}}$	Intensity of PSP at reference condition (count)
I_{TSP}	Intensity of TSP (count)
$I_{\text{TSP}_{\text{ref}}}$	Intensity of TSP at reference condition (count)
I_{ref}	Intensity at reference condition (count)
k	Ratio of temperature-induced intensity change between PSP and TSP
L	Length of the orbiter model (mm)
Ma	Mach number
P	Pressure (kPa)
P_{ref}	Pressure at reference condition (kPa)
P_0	Stagnation pressure (kPa)
P_1	Surface pressure before the shock (kPa)
P_2	Surface pressure after the shock (kPa)
Re	Reynolds number
T	Temperature (K)

T_{ref}	Temperature at reference condition (K)
T_0	Stagnation temperature (K)
t	Time (s)
x	Coordinate in streamwise direction (mm)
y	Coordinate in spanwise direction (mm)
ΔT	Temperature rise (within 3 s) (K)
α	Angle of attack of the orbiter ($^\circ$)

1 Introduction

In the past two decades, the design of future advanced reusable launch vehicle has gradually shifted from single-stage-to-orbit (SSTO) to two-stage-to-orbit (TSTO) concepts, because the latter has shown clear advantages in terms of cost, safety and reliability (Murphy et al. 2004). Clearly, stage separation is a key issue for all TSTO configurations, leading to a critical need to enhance the knowledge base in two-body separation characteristics. Computational works were performed by Moelyadi et al. to investigate the stage separation aerodynamics of a two-stage space transport system in both steady and unsteady cases (Moelyadi et al. 2008a, b). The steady flow patterns show strong interference effects due to incident and reflected shock waves and expansion regions

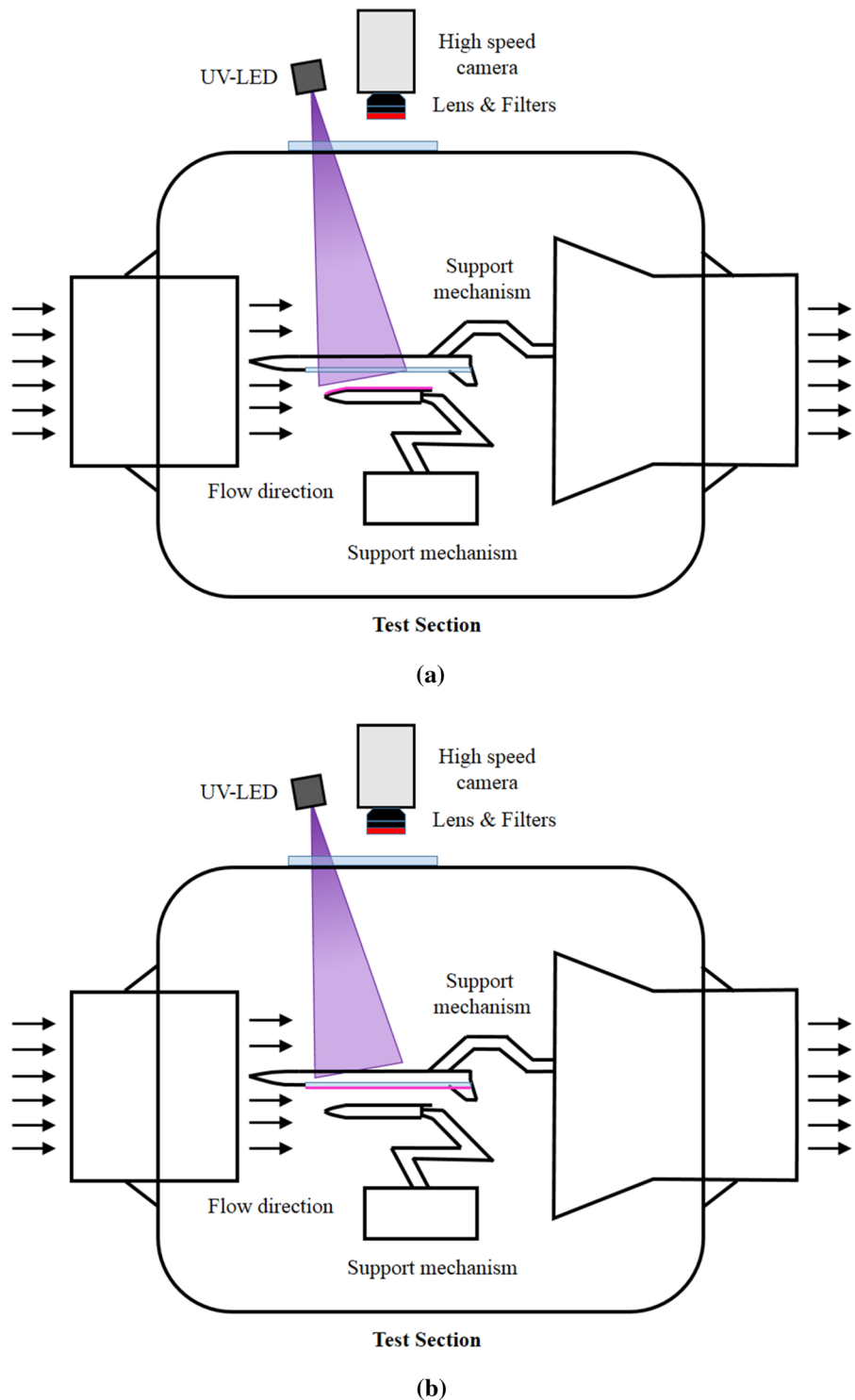
between the carrier and orbital stages. The unsteady simulation results show different characteristics from the steady cases, which is especially evident at the beginning of the separation maneuver. In addition, the accuracy of lift and pitching-moment prediction could be greatly reduced due to errors in simulating shock waves. Fundamental research have shown that severe aerodynamic interference effects are inevitable as the two bodies are in close proximity under supersonic and hypersonic conditions, and the primary interactions were identified to be the strong shock wave impingements from one body onto another. Chaplin et al. (2010) investigated the interaction between two slender bodies at $Ma = 3$. They found that the maximum changes in normal force and pitching moment (induced by shock impingements) equate to an effective incidence of -2.7° and 6° , respectively. Laurence et al. (2007) studied the interaction between two circular cylinders/spheres in hypersonic flow. They found that the interference effects produced substantial lift and drag force on the secondary body downstream, which would be most severe if the secondary body lies completely within the bow shock of the primary body. The dominant mechanism of shock impingement is the interaction between incident shock and boundary layer (SBLI). Early studies showed that SBLI would produce high pressure and strong heating within the shock impingement region, which is of great concern in high-speed flight (Adamson and Messiter 1980; Holden 1986). The unsteady pressure load is another key issue originated from SBLI that is detrimental to aircraft performance and safety (Dolling 2001). Even though accurate predictions of these parameters are challenging, impressive progress has been made in understanding and predicting the problem of low frequency unsteadiness in nominally 2-D interactions, whereas the 3-D situations are yet to be fully explored (Clemens and Narayanaswamy 2014; Gaitonde 2015). Therefore, for two-stage spacecraft with complex geometry, while it is essential to obtain the aerodynamic forces and moments of both bodies during separation through wind tunnel tests, information of flow structures and surface parameters (pressure, temperature, etc.) are equally important to fully understand the complex flow phenomena involving multiple-shock interactions and shock-boundary layer interactions. In this regard, global measurement techniques such as pressure- and temperature-sensitive paints (PSPs and TSPs) are powerful tools for capturing the flow features and the heat transfer characteristics due to their low-intrusiveness and high spatial resolution (Liu and Sullivan 2005).

Since 1990s, PSP and TSP have found applications in hypersonic wind tunnel tests conducted in both short-duration shock tunnels (Borovoy et al. 1995; Hubner et al. 2001) and long-duration blowdown tunnels (Jules et al. 1995; Watkins et al. 2009). Recent developments in fast-responding PSP and TSP have greatly enhanced their measurement capabilities and offered new opportunities for hypersonic

applications (Gregory et al. 2008, 2014; Liu et al. 2019). Porous PSPs with kilo hertz response are now capable of capturing transient pressure features and unsteady pressure fluctuations on model surface. Here, a major issue is the temperature-induced error originated from the fast PSP's temperature sensitivity and the strong heating in hypersonic flow (Peng and Liu 2020). Peng et al. (2016) conducted combined PSP and TSP measurements on an HB-2 model in a $Ma = 5$ flow and obtained transient surface pressure distributions at 0.5 kHz. The accuracy of PSP measurement was significantly improved through a real-time temperature correction method using the TSP data. Recently, Running et al. (2019) used anodized-aluminum (AA) PSP to resolve the surface pressure fluctuations on a blunt cone model at $Ma = 6$. The PSP's frequency response (3 kHz) was sufficient to detect lines of local minimum pressure fluctuation that indicated separation. The temperature correction was performed using the temperature field measured by infrared thermography. Thin-layer TSPs are also fast enough to provide heat flux measurement in high-enthalpy shock tunnels with test durations of a few milliseconds or less. Ozawa et al. (2015) captured the time-resolved temperature field using fast TSP with a sampling rate up to 63 kHz and successfully obtained the heat flux distribution on a transition cone model at $Ma = 7.4$. Issues of test-gas luminosity and particulate-induced dimming were identified, which were mitigated by replacing the erroneous data with interpolated results. The similar method was applied for measurements on an inlet ramp by Laurence et al. (2019). Nonetheless, it should be noted that previous PSP and TSP measurements were mostly conducted on a single model with relatively simple geometry, including additional examples on ramp model (Yang et al. 2012b; Risius et al. 2017) and cone model (Yang et al. 2012a; Juliano et al. 2015). To investigate the interference effects between close bodies in high-speed flows using luminescent coatings, one must first overcome the key issue of limited optical access. For example, Chaplin et al. (2011) studied the interference between two slender bodies in a $Ma = 2.4$ flow using PSP. In that case, it was possible to arrange the light source and camera on one side of the body to capture the side-view PSP images. However, for stage separation studies, the typical configuration involves two mostly flat surfaces with small spacing. It is clearly not feasible to perform PSP measurements on those adjacent surfaces with the previous side-view setup (or any conventional PSP setup).

In the current study, the above technical barrier was overcome and time-resolved PSP and TSP measurements were achieved in a hypersonic flow ($Ma = 6$) on stage separation surfaces with a minimum spacing of 5 mm. As shown in Fig. 1, the multi-body system (including a carrier and an orbiter) was installed upside-down in the wind tunnel. The central area on the bottom side of the carrier

Fig. 1 The schematic of PSP/TSP measurement on adjacent surfaces of **a** the orbiter and **b** the carrier



was fabricated using quartz glass to provide optical access for the interference region. This allowed direct illumination and imaging for measurements on the upper surface of the orbiter (through an optical window on the top of the tunnel as shown in Fig. 1a). More importantly, a unique type of translucent fast PSP was developed, which could be applied on the glass plate and measurements on the carrier could

be realized with a back illumination and imaging setup (see Fig. 1b). It should be noted that this method cannot be implemented using conventional fast PSPs since the lumiphore molecules are usually concentrated near the binder surface (to achieve a fast response) and the binder itself has poor transparency. In addition, a symmetric PSP/TSP configuration was adopted to achieve simultaneous measurements

of surface pressure and temperature, as well as a real-time temperature correction on PSP data. This novel experimental technique provided a valuable solution that allowed investigation on the complex shock–body interactions during steady-state stage separation, as discussed later in this paper.

2 Experimental setup

2.1 Hypersonic facility

The experiment was conducted in a hypersonic testing facility (FL-31) at China Aerodynamics Research and Development Center (CARDC). As shown in Fig. 2, FL-31 is a blow-down wind tunnel with vacuum suction to produce hypersonic flow of $Ma = 5\text{--}9$. This tunnel mainly consists of a high-pressure gas source (with valves), a metal-plate heater (with thermal valves), a stabilizing section (with nozzle), a test section, a diffuser, a vacuum system and an electrical control system. Test model is mounted on a support mechanism with variable angle of attack. A pair of optical windows ($\Phi 400$ mm) is located on the side walls of the test section for visualization of flow structure using Schlieren technique. Another window ($\Phi 300$ mm) is located on top of the tunnel to provide optical access for PSP and TSP measurements.

2.2 Translucent pressure- and temperature-sensitive paints

The PSP in this work features a novel formulation which uses mesoporous, hollow silicone dioxide particles as hosts for luminescent molecules. During its fabrication, 40 mg polystyrene, 150 mg mesoporous particles (from Suzuki Yushi Industrial Co. Ltd.) and 1 mg luminophore (PtTFPP, Frontier Scientific) are first added into 1 ml of dichloromethane, and then 1–2% dispersant (Tween 80, Guangdong Runhua Chemistry) is added to the mixture to form a slurry. The slurry is sonicated for 10 min before it is sprayed onto the model surface using an airbrush. The typical paint thickness and surface roughness were

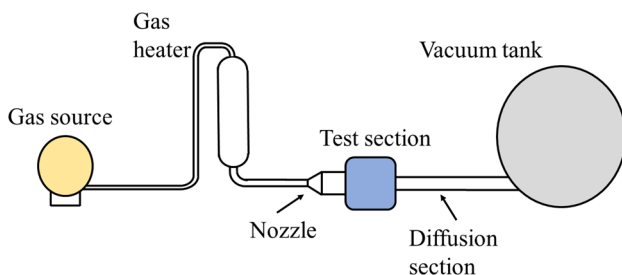


Fig. 2 The schematic of $\phi 0.5$ m hypersonic wind tunnel at CARDC

20 μm and 5 μm , respectively. This mix-and-spray method results in a fairly uniform luminophore distribution from top to bottom as shown in Fig. 3a. Such a luminophore distribution is crucial to achieve a translucent coating that remains functional for a back-illumination and imaging configuration. Meanwhile, the particle's highly porous and hollow structure greatly facilitates oxygen diffusion inside the PSP binder, which results in a response time of around 100 μs (Peng et al. 2018). Figure 4 shows the dynamic calibration results obtained by using a shock tube. The step response (90% rise time) of this paint was 106, 86 and 137 μs for paint thickness of 20, 50 and 100 μm , respectively. In comparison, the conventional polymer–ceramic (PC) PSPs usually have luminophores deposited near the binder surface to achieve fast response (see Fig. 3b). According to our previous study (Jiao et al. 2018), the transmittance of an 11.7- μm -thick PC binder is about 20% at 650 nm (emission wavelength) and less than 10% around 405 nm (excitation wavelength). For PC-PSP with a paint thickness of 20 μm , the signal attenuation with back-illumination and imaging configuration is over 98% (estimated as $1 - 20\% * 10\% = 98\%$). The amount of signal attenuation can be reduced to about 85% for a 4.0- μm -thick binder, but the reduction in binder thickness leads to signal loss as well. Therefore, the strong light attenuation of the binder

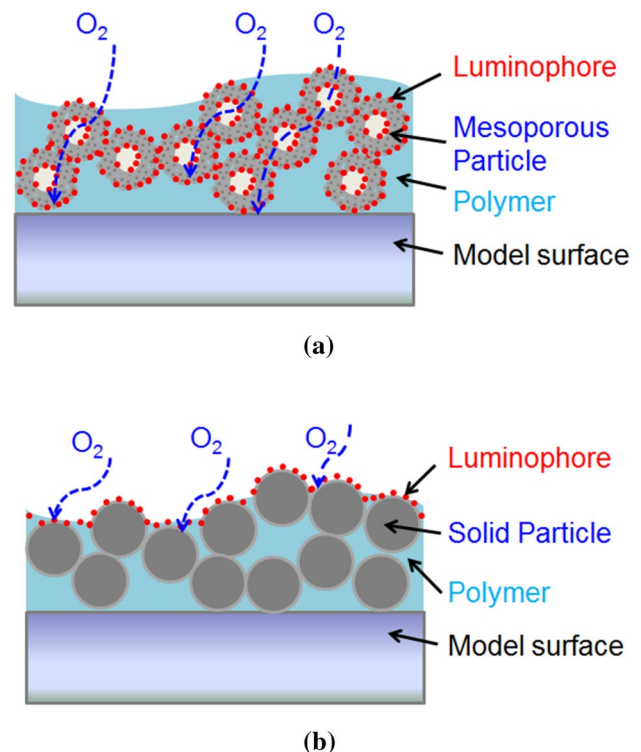


Fig. 3 Microstructures of **a** mesoporous-particle PSP and **b** conventional polymer–ceramic PSP

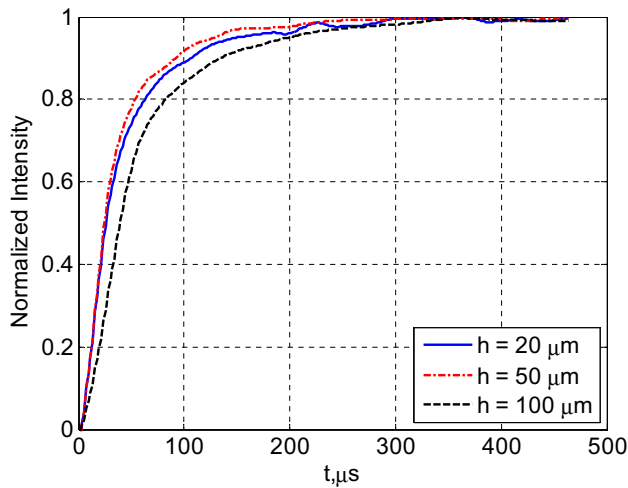


Fig. 4 Step response of PSP samples with different thickness

leads to insufficient signal level for the back-illumination and imaging configuration. In addition, the mesoporous-particle PSP (MP-PSP) has shown clear improvements in photostability and paint durability over the conventional PC-PSP, which provides benefits in high-speed, unsteady aerodynamic testing (Peng et al. 2018).

The TSP uses an oxygen-impermeable automobile clearcoat (DupontChromClear HC7776S) as the binder and $\text{Ru}(\text{dpp})_3$ (from J&K Scientific) as the temperature sensor. The binder was firstly mixed with luminophore solution with a concentration of 2 mg/ml, and then, the mixture was air-sprayed onto the model surface. The resulting paint thickness was within 20 μm , and the surface roughness was 1–2 μm . The TSP is also translucent and allows illumination and imaging from backside.

The absorption and emission spectrum of PSP and TSP are shown in Fig. 5. The absorption spectrum data are taken from the thesis work by Sakaue (2003), and the emission spectrum data were measured by a spectrometer (USB 2000, Ocean Optics) under the excitation of a 405-nm UV-LED (UHP-T-LED-405-EP, Prizmatix). The PSP and TSP have overlapping absorption spectrum around 400 nm, proving that the combined paint system can be excited efficiently using the current light source, which has a full-width half-maximum of 16 nm as indicated by the purple region in Fig. 5. A 550-nm long-pass filter was selected for measurement to exclude the excitation light while maintaining most of PSP and TSP signals, as indicated by the yellow line in Fig. 5. In addition, the current luminophore concentrations in the solution of PSP and TSP resulted in similar intensity levels under the test condition. The average signal level of PSP was about 20% stronger than the TSP for a typical set of wind-on images.

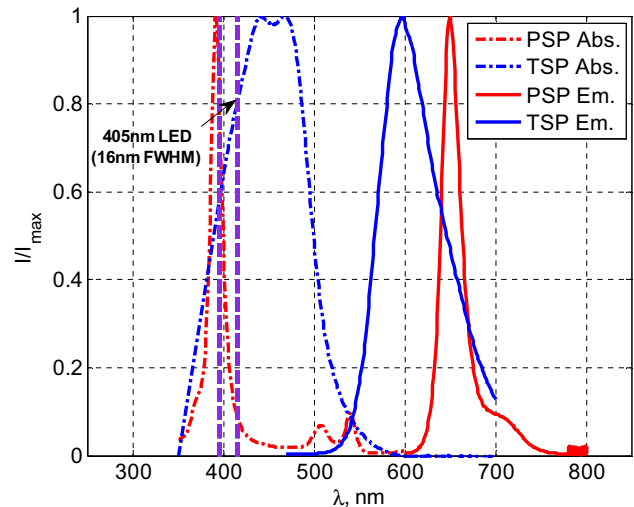


Fig. 5 Absorption and emission spectrum of PSP and TSP

2.3 Test model and measurement system

The schematics of the orbiter model and the carrier model are shown in Fig. 6a, b, respectively. The orbiter model with a length of 0.22 m was made of aluminum, and its surface was applied with a matt finish to minimize light reflection. A total of 27 pressure taps were installed on the model with the exact locations shown in Fig. 6a. The carrier model was fabricated in the same way as the orbiter model, except for the center area which was

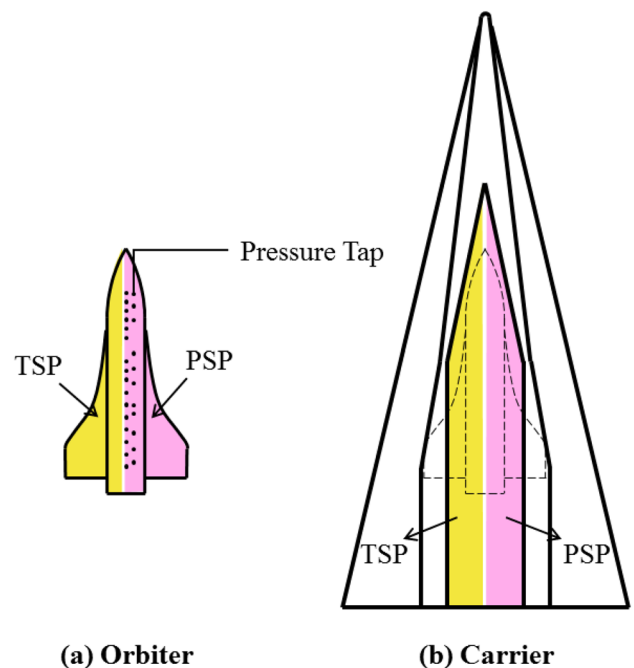


Fig. 6 Schematic of the test model showing the PSP and TSP regions: **a** the orbiter, **b** the carrier

replaced by a glass plate to provide optical access for the interference region. This flat glass plate was flush-mounted on the carrier model and was fixed by a total of 14 screws distributed near the edge. No transducers were installed on the glass plate to avoid any possible blockage. The PSP and TSP were applied symmetrically from the centerline to the wing tip on the lower surface of the orbiter, but only the main body and the wing root areas could be observed through the glass plate installed on the carrier. The coatings were removed after the measurements were completed on the orbiter. Then, the PSP and TSP were applied symmetrically on the glass plate for measurements on the carrier.

During wind tunnel experiments, both the orbiter and carrier were mounted up-side down on two support systems in the test section. The vertical location and the angle of attack of the orbiter could be adjusted to achieve the desired test conditions listed in Table 1. It should be noted that a positive angle of attack corresponded to the nose-up condition of the orbiter in the current up-side down setup. Continuous illumination for PSP and TSP was provided by the 405-nm LED through a glass window on top of test section. The luminescent signal was recorded by a 12-bit high-speed camera (SA-4, Photron) at 3 kHz through a 50-mm lens and a 550-nm long-pass filter. The exposure time was 300 μs for each frame, and the spatial resolution was 0.32 mm/pixel. A total of 100 reference images were recorded prior to each run with a static pressure around 1 kPa, and then, the averaged image was calculated for further data processing. The wind-on images were captured continuously after the steady flow condition was reached at Ma = 6, resulting in more than 10,000 steady-flow images in each case. The pressure taps were connected to a transducer module (64HD-10psi, PSI) with a sampling rate of 200 Hz.

3 Data processing

3.1 A-priori temperature calibration

The temperature calibrations of both PSP and TSP were performed in a calibration device (HCP621-Cust, INSTEC.) with a pressure range from 20 to 200 kPa and a temperature range from 0 to 873 K. Paint samples were prepared on 1 cm diameter aluminum coupons. The measurement system was identical to the one used for wind tunnel tests, except for the imager which was replaced by a low frame-rate camera (pco. 1600, pco imaging). The temperature range of calibration was from 283 to 353 K, with a reference temperature of 303 K. The pressure was set to the minimum value (20 kPa) during the calibration to approximate the wind tunnel environment. As shown in Fig. 7a, nonlinear relations were found between intensity and temperature for both paints, which could be fitted by polynomial curves. Figure 7b shows the variation of *k* value with respect to temperature. Here, *k* is the ratio of PSP and TSP intensity changes caused by temperature, which is a key parameter for temperature correction as discussed in the following section.

3.2 In situ pressure calibration with temperature correction

For PSP measurements on the orbiter, in situ calibrations were applied using the pressure tap data in each case respectively. In general, the temperature variations on the orbiter were relatively small due to weaker shock-body interactions (compared with the carrier as discussed later). Therefore, the quality of in situ calibration was satisfactory as shown by one exemplary case (*h* = 11.3 mm, $\alpha = 0^\circ$) in Fig. 8a. However, for the test case with the minimum separation distance, the temperature induced errors became obvious due to increased shock strength. As shown in Fig. 8b, the data points were more scattered due to the fact that the PSP data within the regions of shock impingement were biased

Table 1 Test conditions of PSP and TSP measurements

Case #	Ma	P_0 (MPa)	T_0 (K)	Re	Model	<i>h</i> / <i>L</i>	α (°)
1	6	1.89	492	3.56×10^6	Orbiter	0.121	0
2						0.051	0
3						0.023	0
4						0.051	2
5						0.051	-2
6					Carrier	0.121	0
7						0.051	0
8						0.023	0
9						0.051	2
10						0.051	-2

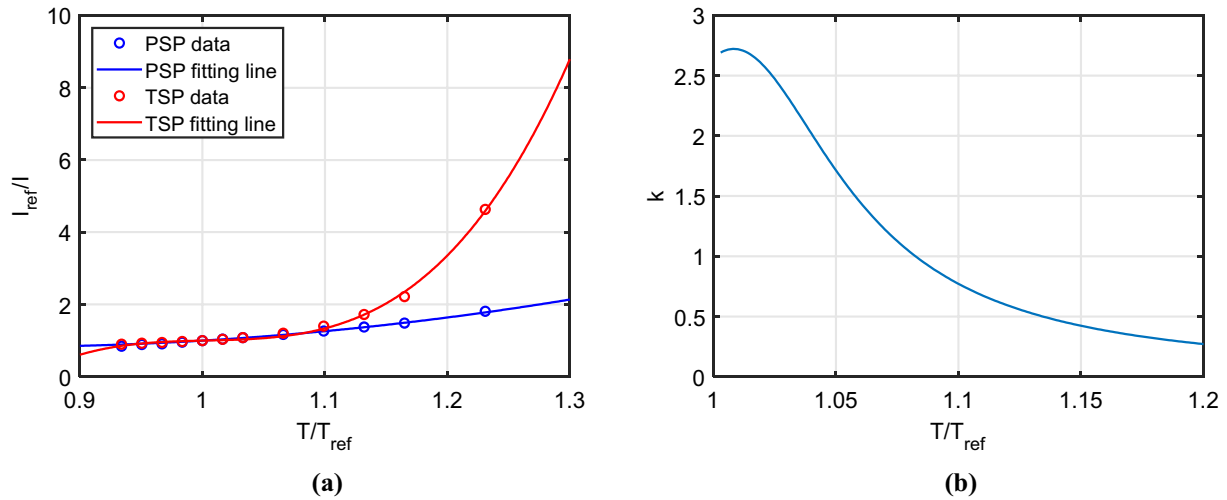


Fig. 7 Temperature calibration results: **a** calibration curves, **b** temperature dependence of k

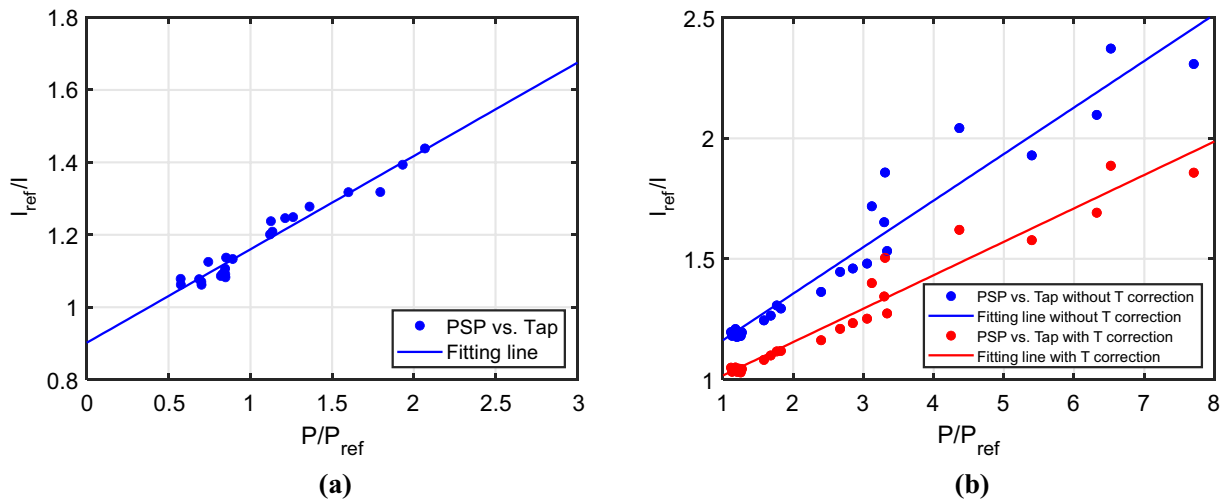


Fig. 8 In situ calibration results of **a** test case 2 and **b** test case 3

(to higher values of intensity ratio) due to significant temperature rise. With the simultaneous TSP measurement, this issue could be resolved by applying temperature correction on the PSP data based on the following equation (Peng et al. 2016):

$$\frac{I_{ref}}{I} = \frac{I_{PSP_ref}/I_{PSP}}{\left(\left(I_{TSP_ref}/I_{TSP} - 1 \right) \times k(T) + 1 \right)} \quad (1)$$

where k was the ratio of temperature-induced intensity change between PSP and TSP obtained from calibration (see Fig. 7b). The quality of in situ calibration was clearly improved after temperature correction according to the comparison in Fig. 8b. The remaining biases of the

corresponding data points were likely due to some paint damage during the flow build-up stage. This temperature correction method was applied to all test cases to further improve the accuracy of PSP measurement.

For PSP measurements on the carrier, it was not possible to directly implement in situ calibration due to the lack of pressure transducer data. Considering that the reference images of all test cases were taken at similar pressure and temperature conditions, the calibration results of the orbiter were applicable to the carrier cases. Here, the calibration data of test case 3 were selected since it covered the widest pressure range. Temperature correction was also performed on the PSP data of the carrier cases before they were converted to pressure using the calibration curve.

3.3 Image processing method

The data processing of PSP and TSP images was performed in MATLAB. The procedures are summarized in Fig. 9, which include four main steps: image registration, intensity ratio calculation, restoration of image defects and intensity-to-pressure/temperature conversion. The intensity-based registration function “imregister” was used for image registration. This MATLAB function is built on intensity-based image registration algorithms, which can handle translation, rotation and scale of both 2D and 3D images. The image defects, which were mostly due to the paint damages generated by strong shock impingement, could be restored using a Gaussian filter method with a 7 by 7 pixel window. However, the algorithm was unable to restore a few large defects caused either by signal contamination from adhesives or accidental blockage from fallen paint chips. The signal contaminations from adhesives existed on the orbiter side causing six circular defects in TSP images as shown in Figs. 17 and 18. This issue was insignificant for PSP results since the PSP coating had less transparency than the TSP coating. The accidental blockage from fallen paint chips only occurred in test case #5, causing a few random defects as shown in Figs. 12c and 18c. Finally, the restored images were converted to pressure and temperature fields using the calibration results. For PSP images, the temperature correction was applied prior to the implementation of the in situ calibration as previously discussed. Both the time-averaged pressure and the pressure fluctuations were calculated based on a total of 3000 images (over 1 s duration of steady flow).

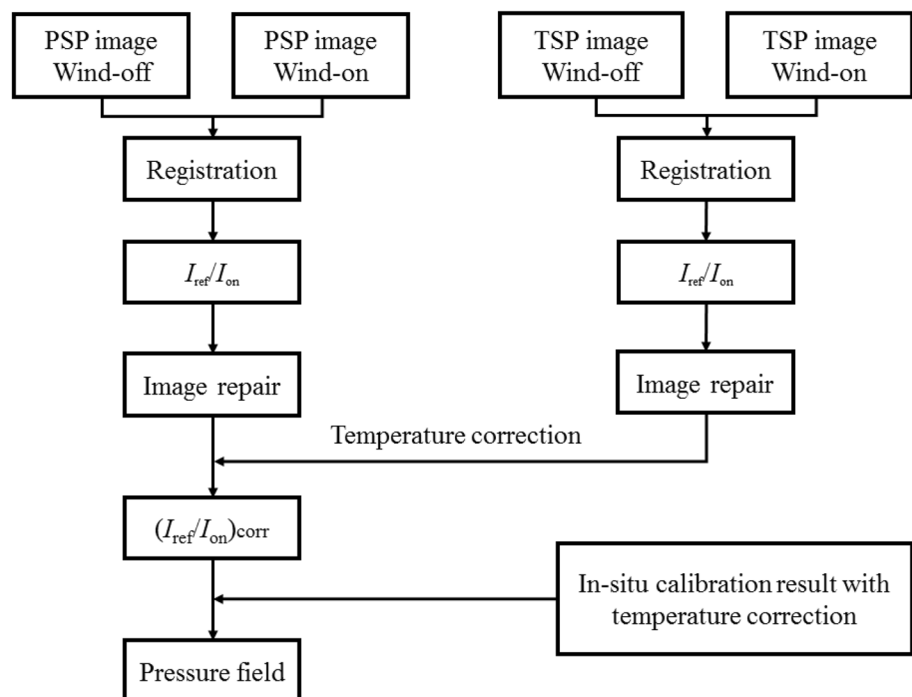
The TSP images were processed individually and the results were shown in the form of temperature rise (ΔT) for a 3 s duration, allowing direct comparisons of heat transfer rate. In addition, a mirror operation was performed on each result to yield a complete field of pressure or temperature. Here, the slightly asymmetrical PSP and TSP coated regions led to a narrow gap near the centerline as shown in some test cases.

4 Results and discussion

4.1 Typical flow structures

A full view of the flow field for $h/L=0.121$ and $\alpha=0^\circ$ are shown by the Schlieren image on the left side of Fig. 10. The shock waves are firstly generated by the carrier nose, which propagates downstream on both sides of the model. Then, the focus is placed on the flow structure within the interaction region between the carrier and the orbiter. Here, the main shock wave structure is originated from the orbiter nose which has two downstream reflections. The first reflection is in the central region on the carrier side, and the second reflection is at the end of the orbiter region. The location of two shock impingements agrees well with the sharp pressure increases in PSP results as shown on the right side of Fig. 10. The PSP results on the carrier side also show a clear 3D shock structure, which is generated by the 3D shape of the orbiter nose. On the orbiter side, the high-pressure region near the nose is captured with some data missing at the tip due to paint damage. A few additional shock waves

Fig. 9 Data processing procedures of PSP and TSP images



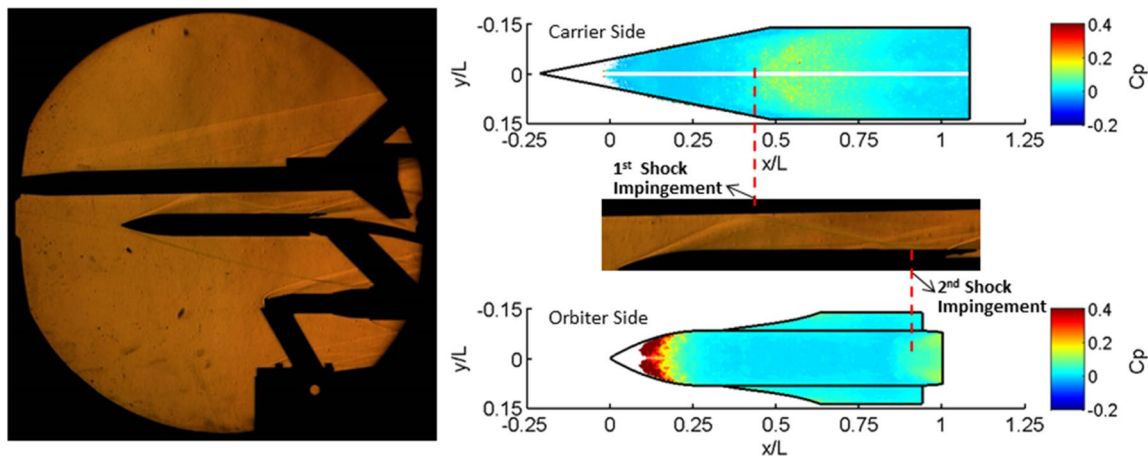


Fig. 10 PSP and Schlieren results showing the flow structure at $h/L=0.121$

are visible on the latter half of the interaction region. Those are likely generated by the wing of the orbiter, since the corresponding pressure features are not found in the PSP results.

4.2 Time-averaged and unsteady PSP results

The time-averaged pressure fields for three separation distances and three inclined angles are compared in Figs. 11 and 12, respectively. The C_p contours on the left are featured by symmetrical high-pressure regions due to shock impingements on both sides. The location, size and magnitude of these regions are highly sensitive to the geometrical arrangements of the orbiter and the carrier. While the pressure contours provide a direct view of the 3D flow fields, it is important to extract some representative data (e.g., pressure on the centerline) that facilitate further analysis on shock impingement. Accordingly, the C_p distribution along the centerline for each case is displayed on the right along with the derivatives (with respect to x/L) for locating shock impingements. The pressure tap data on the orbiter side are also included showing fairly good agreement with the PSP data in all cases. Quantitative comparisons regarding the location and strength of shock impingement are presented in Fig. 13. Here, the exact shock locations are determined based on the peaks of $d(C_p)/d(x/L)$, and the shock strengths are evaluated by the pressure ratios across the shock impingement.

The flow field between the two models clearly becomes more complex as the separation distance decreases. In particular, the first shock impingement moves upstream on the carrier side with an enhanced strength. This variation in shock location is obviously due to the geometrical relations between the shock wave and the two surfaces. The variation in shock strength is also not surprising considering that the shock strength is reduced during its expansion

from the tip of the orbiter nose. This decaying effect is less for small separation distance which results in a stronger shock impingement. After the first impingement, the shock is reflected between both sides and the number of reflection clearly increases as the orbiter moves closer to the carrier. Meanwhile, the pressure peaks shift upstream on the orbiter leading to a pitch down moment (for the current up-side down configuration). Significant decay in reflected shock strength is observed for each case as well, especially for the first two reflections as shown in Fig. 13a.

For the test cases with different inclined angle, the flow fields have some similarity with four discernible shock impingements in each case. However, the quantitative results in Fig. 13b clearly reveal some differences in both shock location and strength. The location of first shock impingement (on the carrier side) moves upstream as α increases. This is attributed to the effect of separation distance, because a larger α leads to a smaller separation distance at the tip. The pressure peaks move upstream on the orbiter for the same reason, which lead to a pitch down moment for a positive α , and a pitch up moment for a negative α . Meanwhile, the shock strength does not show a clear trend. For the case of $\alpha = 2^\circ$, the first shock impingement is the strongest, but the subsequent ones are significantly weaker than the other two cases. In contrast, the case of $\alpha = -2^\circ$ shows the strongest shock impingements except for the first one. These behaviors can be explained by the underlying mechanisms as discussed in the following paragraph.

Based on the results, two main factors responsible for shock strength variations (during shock impingements) are identified: (1) inclined angle of the orbiter and (2) distance from the orbiter nose to the impingement point. The first one determines the original strength of the shock, and the second one determines the amount of decay in shock strength. As the separation distance h/L increases (for a fixed

Fig. 11 Time-averaged PSP results at $\alpha=0^\circ$: **a** $h/L=0.121$, **b** $h/L=0.051$ and **c** $h/L=0.023$

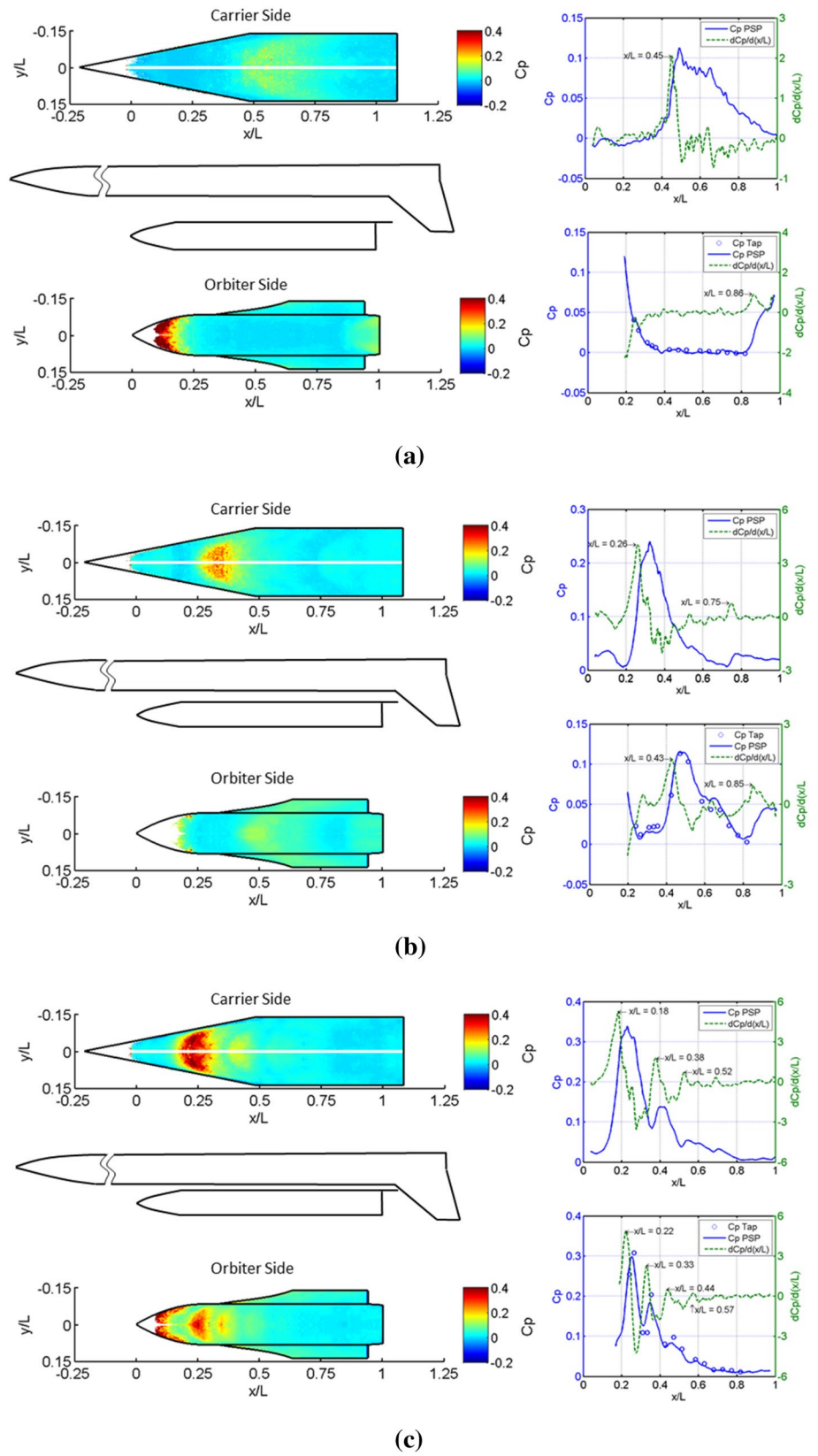
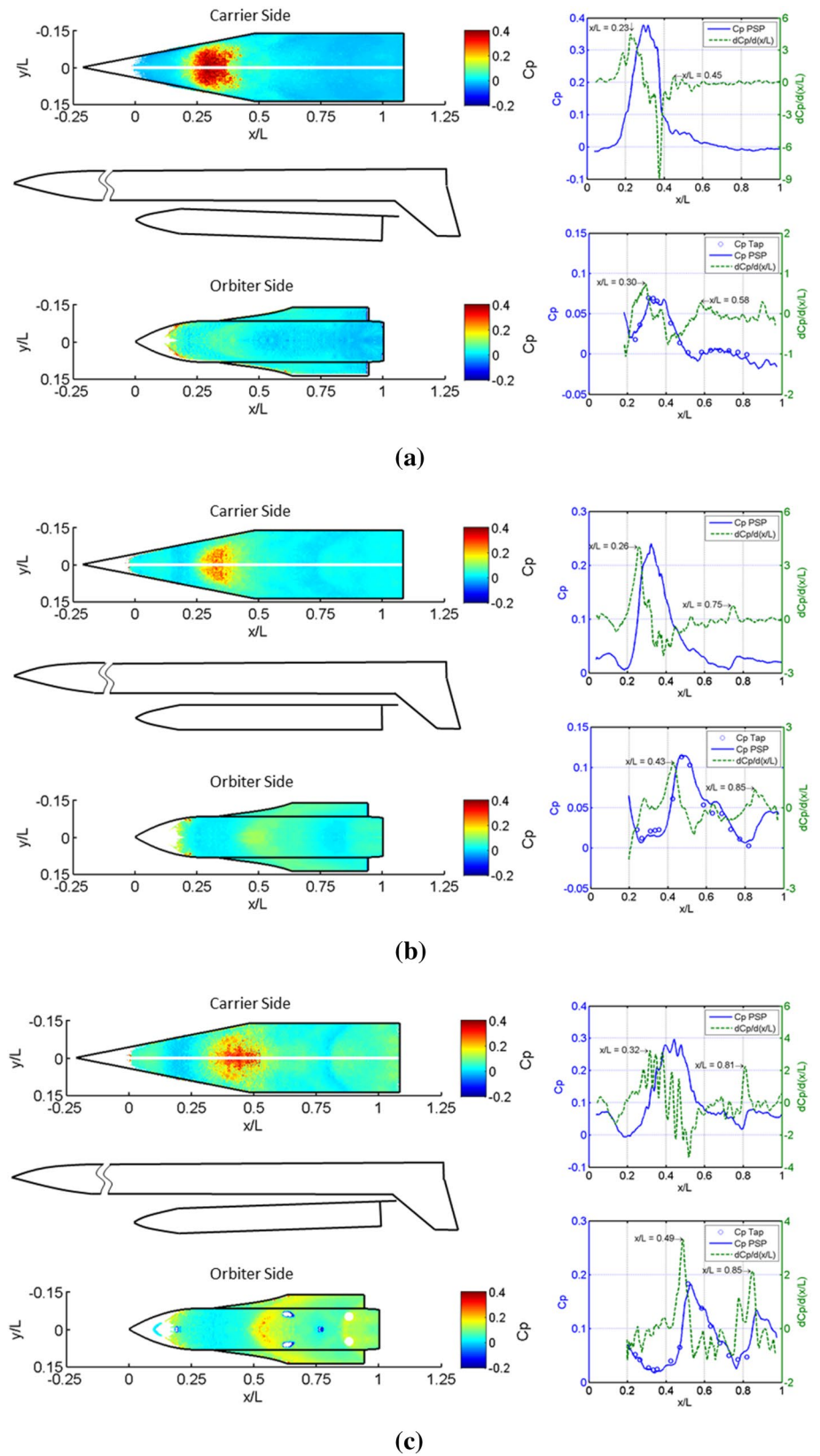


Fig. 12 Time-averaged PSP results at $h/L=0.051$: **a** $\alpha=2^\circ$, **b** $\alpha=0^\circ$ and **c** $\alpha=-2^\circ$



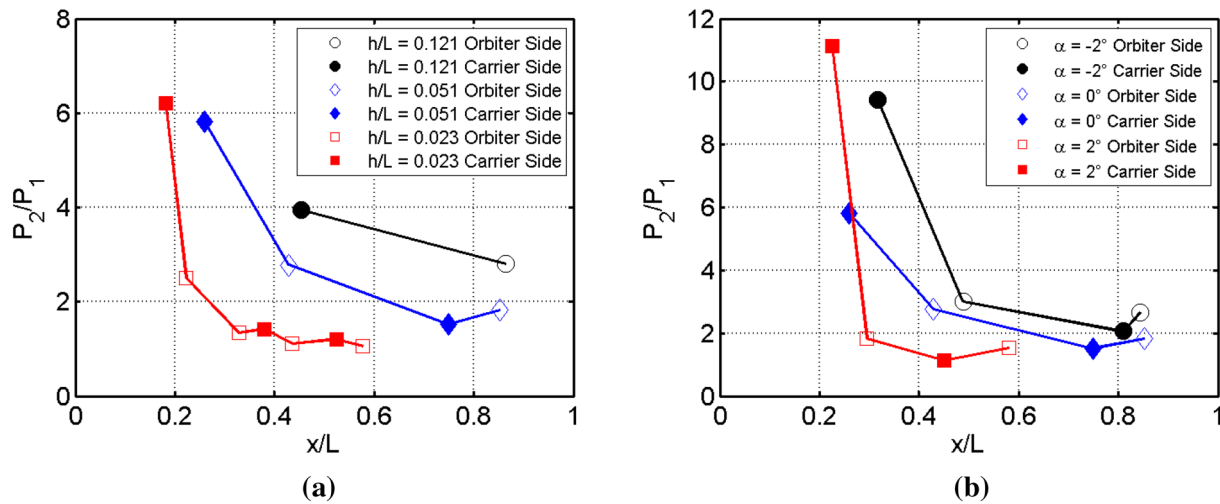


Fig. 13 Comparison of shock location and strength showing **a** effects of separation distance and **b** effects of inclined angle

inclined angle α), the shock has the same initial strength but experiences larger decay before reaching the carrier, leading to less pressure rise for the first impingement on the surface (as shown in Fig. 13a). As α varies for a fixed h/L , the situation is more complex since both factors contribute. A larger α would generate a weaker shock with a shorter travel distance. This means that these factors have offsetting effects, and therefore, no clear trend can be seen from Fig. 13b for the first impingement. There is actually an additional factor that affects the decay in reflected shocks, which is the duct geometry between models. For $\alpha = 2^\circ$, the models form a diverging duct which facilitates the decay of shock waves due to expansion effect (Nettleton 1973). For $\alpha = -2^\circ$, the models formed a converging duct which would reduce the decay of shock waves due to compression effect. Therefore, the decay rate of shock strength increases with inclined angle, which leads to clearly different variations in reflected shock strength as shown in Fig. 13b. The current finding is consistent with previous results from the numerical simulation of stage separation (Moelyadi et al. 2008b) and the experimental study of slender multi-body interactions (Chaplin et al. 2011).

The time-resolved PSP results are presented in terms of root-mean-square pressure coefficient (C_{pstd}) to evaluate the flow unsteadiness. The C_{pstd} distributions on the carrier side for different separation distance are compared in Fig. 14. The region of increased pressure fluctuation level agrees well with the shock impingement locations, and the fluctuation level increases with the strength of shock impingement. Figure 15 compares the C_{pstd} distributions extracted from the centerline. In each case, the peak location of pressure fluctuation coincides with the pressure peak of the first shock impingement. The pressure power spectra are calculated and shown in Fig. 16 to further identify the

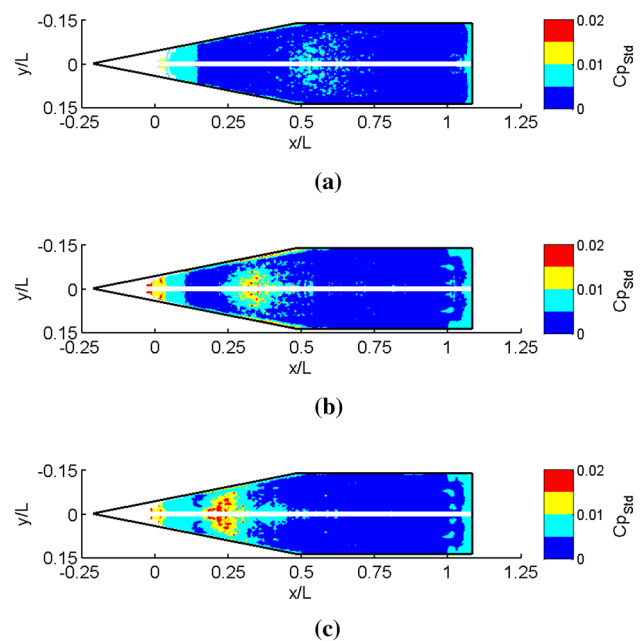


Fig. 14 Pressure fluctuation levels on the carrier side at $\alpha = 0^\circ$: **a** $h/L = 0.121$, **b** $h/L = 0.051$ and **c** $h/L = 0.023$

source of increased pressure fluctuation. Peaks are clearly observed at $f = 134$ Hz and its harmonics near the shock impingement location, and magnitude increases with shock strength. Considering that this peak frequency is constant for all cases, it is very likely due to shock movement induced by model vibration. In contrast, the broadband low-frequency unsteadies related to shock/boundary-layer interaction cannot be identified from the power spectra, indicating that the effect of shock-induced separation is limited (Dupont et al. 2005; Clemens and Narayanaswamy 2014). In addition, the

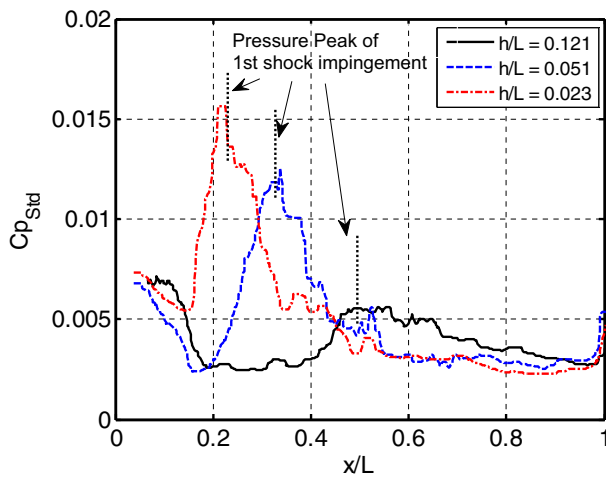


Fig. 15 Distributions of pressure fluctuation levels near the centerline on the carrier side ($\alpha=0^\circ$)

pressure fluctuation level increases slightly near both ends of the measured region, which is likely due to the insufficient excitation light and poor signal-to-noise ratio of PSP data. The pressure fluctuation levels are significantly less on the orbiter side due to weaker shock strength. The results generally lack clear features and are therefore not shown.

4.3 TSP results

While the TSP results are vital for applying temperature correction on PSP data, they can offer some insights on the heat transfer characteristics as well. The temperature rise (ΔT) during the steady flow for three separation distances and three inclined angles are compared in Figs. 17 and 18, respectively. The corresponding ΔT distributions along the centerline were calculated and compared in Figs. 19 and 20, respectively. The first observation is that the carrier side generally has larger temperature rise than the orbiter side, which is due to the different materials being used (quartz glass for the carrier side and aluminum for the orbiter side). These two materials have similar heat capacity (700 J/kg K for quartz glass and 921 J/kg K for aluminum), but aluminum has significantly higher heat conductivity (236 W/m K) than quartz glass (1.05 W/m K) which leads to stronger heating and higher surface temperature. On the carrier side, the most prominent feature in each case is the strong heating due to the first shock impingement. The location of the peak ΔT agrees well with the pressure peak, which is slightly shifted downstream from the previously determined shock impingement point. Meanwhile, the variation trends regarding the peak location and magnitude are generally consistent with the findings in PSP results. In overall, the case of $h/L=0.051$ and $\alpha=-2^\circ$ shows the strongest heating mostly due to the compression effect within the converging interaction region.

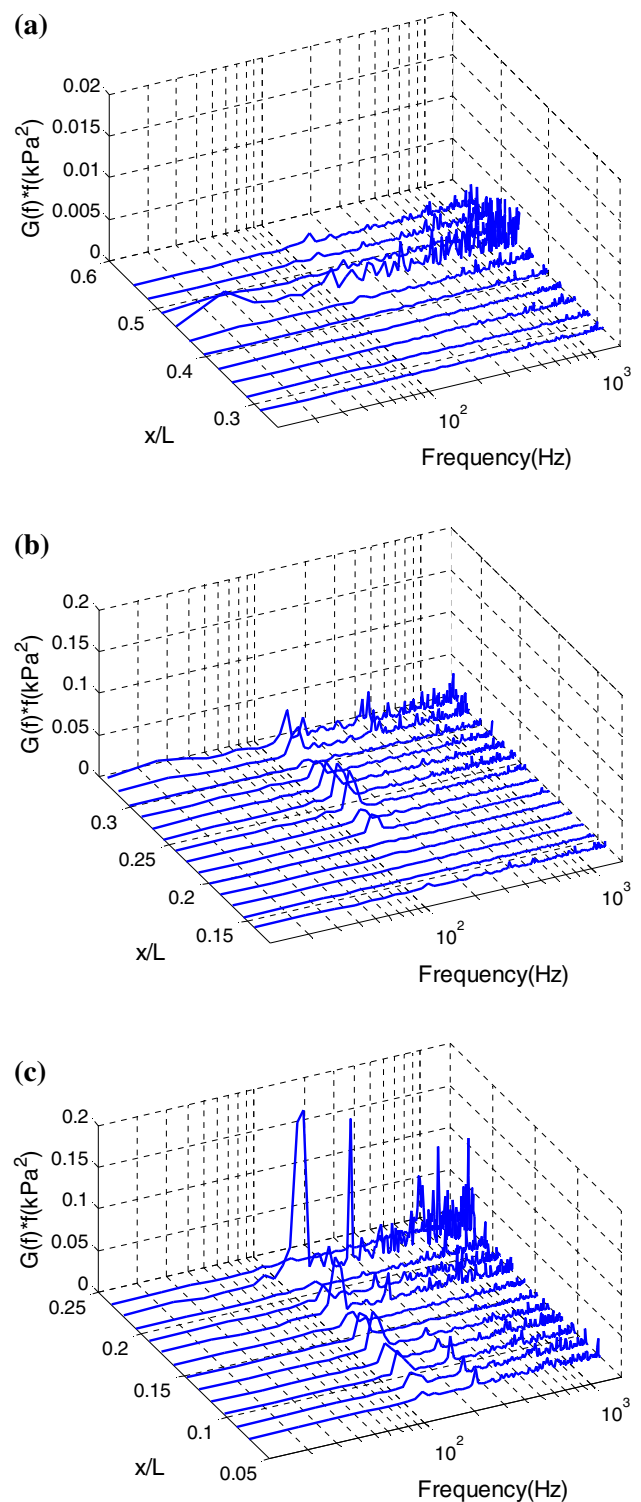


Fig. 16 Pressure power spectra near the centerline on the carrier side at $\alpha=0^\circ$: **a** $h/L=0.121$, **b** $h/L=0.051$ and **c** $h/L=0.023$

On the orbiter side, there is strong heating on the orbiter nose which essentially functions as a 3D ramp for the upcoming flow. In the nose region, the magnitude

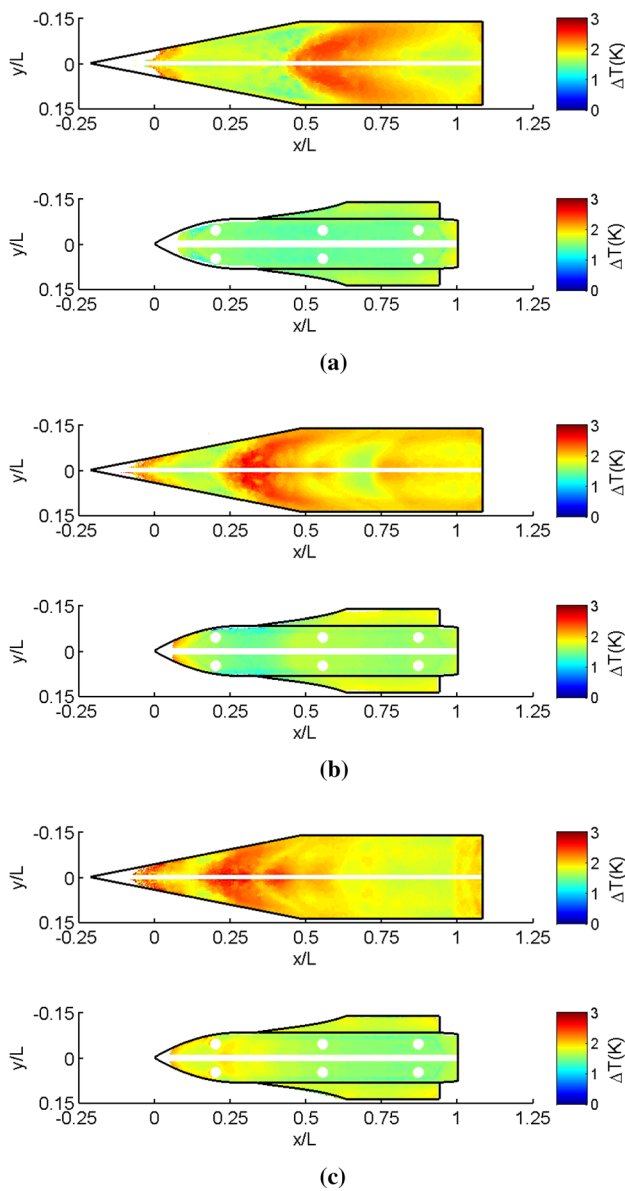


Fig. 17 TSP results of different separation distance at $\alpha=0^\circ$: **a** $h/L=0.121$, **b** $h/L=0.051$ and **c** $h/L=0.023$

of ΔT increases as the separation distance/inclined angle reduces, which is due to a stronger compression effect. The heating due to shock impingement is relatively weak since there is significant decay in shock strength after the first impingement on the carrier side. Again, the variation trend regarding the peak location and magnitude agrees well with the findings in PSP results. In addition, an increase in ΔT is generally observed in the wing root region, which is related to the low heat capacity of the thin wing section.

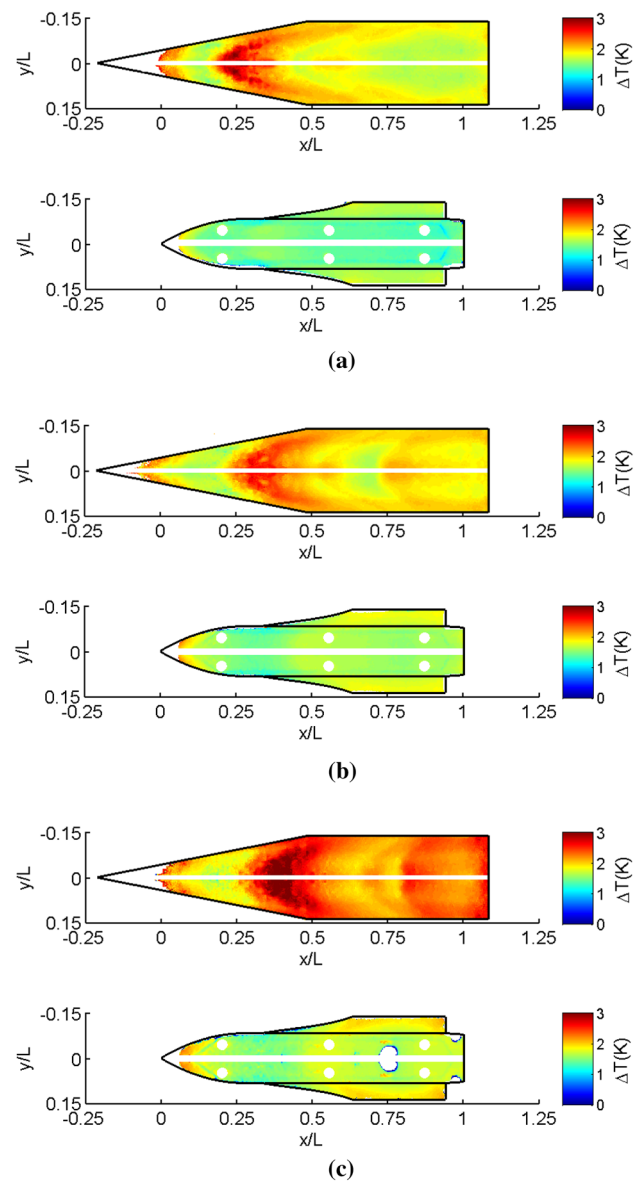


Fig. 18 TSP results of different inclined angle at $h/L=0.051$: **a** $\alpha=2^\circ$, **b** $\alpha=0^\circ$ and **c** $\alpha=-2^\circ$

5 Conclusions

The key issue of optical access in experimental investigation of hypersonic stage separation has been resolved by implementing a translucent PSP and TSP system with back-illumination and imaging capability. Meanwhile, the temperature-induced error in PSP measurement was compensated by applying an in situ calibration with temperature correction from TSP results. With this technique, time-resolved pressure and temperature on adjacent surfaces between the orbiter and the carrier were obtained in a Mach 6 flow. The location and strength of shock

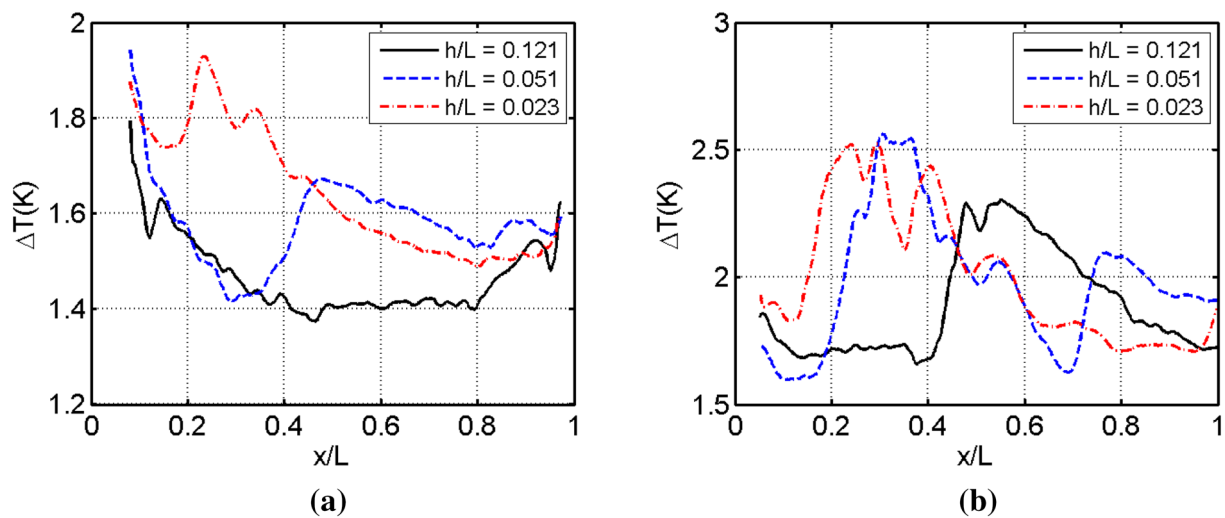


Fig. 19 Distributions of ΔT near the centerline at $\alpha = 0^\circ$: **a** orbiter side and **b** carrier side

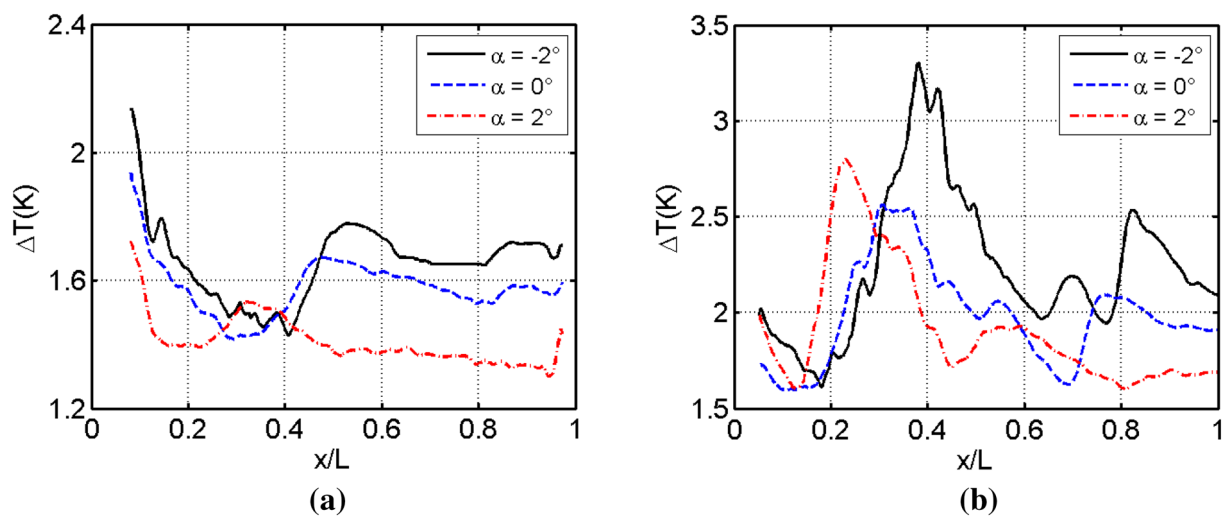


Fig. 20 Distributions of ΔT near the centerline at $h/L = 0.051$: **a** orbiter side and **b** carrier side

impingement, pressure fluctuation levels, as well as heat transfer features were clearly captured. The main findings include:

1. The dominant flow feature of the interaction region is the shock wave generated by the pointed orbiter nose, which initially impinges on the carrier side with subsequent reflections between the adjacent surfaces.
2. Smaller separation distance leads to a more complex shock structure with a stronger initial shock impingement and increased number of reflections afterwards. The pressure and temperature peaks generally move upstream as separation distance reduces.
3. The inclined angle not only changes the locations of shock impingement, but also greatly affects the decay

rate afterwards. For a positive angle of attack (of the orbiter), the shock structure moves upstream with a faster decay rate due to the expansion effect of the diverging interaction region. For a negative angle of attack, the shock structure moves downstream with stronger reflected shocks due to the compression effect of the converging interaction region.

4. The major source of pressure fluctuation is the shock movement induced by model vibration at a certain frequency (134 Hz), and the fluctuation level increases with shock strength. There is no clear sign of shock-induced separation in the PSP results.

The current PSP/TSP measurement technique has offered unique capability for in-depth flow diagnostics

in stage-separation research. In future work, it should be supplemented by other flow visualization techniques (Schlieren, oil-film, etc.) to fully understand the complicated shock-wave/boundary layer interaction within narrow spacing. The application should also be extended to unsteady test conditions for investigating dynamic stage-separation problems. In addition, even though the MP-PSP has shown improvements in paint robustness over conventional PC-PSP (Peng et al. 2018), paint damages were still observed near the nose region or under strong shock impingements. Further advances in paint formulation are still desired to cope with the hostile environment in hypersonic ground testing facilities.

Acknowledgements This work was supported by National Natural Science Foundation of China (NSFC Nos. 11725209 and 11872038) and funding from Gas Turbine Research Institute of Shanghai Jiaotong University.

References

- Adamson TC Jr, Messiter AF (1980) Analysis of two-dimensional interactions between shock waves and boundary layers. *Ann Rev Fluid Mech* 12:108–138. <https://doi.org/10.1146/annurev.fl.12.010180.000535>
- Borovoy V, Bykov A, Mosharov V, Orlov A, Radchenko V, Phonov S (1995) Pressure sensitive paint application in shock wind tunnel. In: Proceedings of the 16th international Congress on instrumentation in aerospace simulation facilities
- Chaplin RA, MacManus DG, Birch TJ (2010) Aerodynamic interference between high-speed slender bodies. *Shock Waves* 20:89–101. <https://doi.org/10.1007/s00193-009-0241-7>
- Chaplin R, MacManus D, Leopold F, Gauthier T, Martinez B, Birch T (2011) Experimental investigation into the interference aerodynamics of two slender bodies in close proximity. *Exp Fluids* 50:491–507. <https://doi.org/10.1007/s00348-010-0946-5>
- Clemens NT, Narayanaswamy V (2014) Low-frequency unsteadiness of shock wave/turbulent boundary layer interactions. *Ann Rev Fluid Mech* 46:469–492. <https://doi.org/10.1146/annurev-fluid-010313-141346>
- Dolling DS (2001) Fifty years of shock-wave/boundary-layer interaction research: what next? *AIAA J* 39:1517–1531. <https://doi.org/10.2514/2.1476>
- Dupont P, Haddad C, Ardisson JP, Debiève JF (2005) Space and time organisation of a shock wave/turbulent boundary layer interaction. *Aerosp Sci Technol* 9:561–572. <https://doi.org/10.1016/j.ast.2004.12.009>
- Gaitonde DV (2015) Progress in shock wave/boundary layer interactions. *Prog Aerosp Sci* 72:80–99. <https://doi.org/10.1016/j.paero.2014.09.002>
- Gregory JW, Asai K, Kameda M, Liu T, Sullivan JP (2008) A review of pressure-sensitive paint for high-speed and unsteady aerodynamics. *Proc Inst Mech Eng G J Aerosp* 222:249–290. <https://doi.org/10.1243/09554100JAERO243>
- Gregory JW, Sakaue H, Liu T, Sullivan JP (2014) Fast pressure-sensitive paint for flow and acoustic diagnostics. *Ann Rev Fluid Mech* 56:303–330. <https://doi.org/10.1146/annurev-fluid-010313-141304>
- Holden MS (1986) A review of aerothermal problems associated with hypersonic flight. In: 24th AIAA aerospace sciences meeting, AIAA-86-0267
- Hubner JP, Carroll BF, Schanze KS, Ji HF, Holden MS (2001) Temperature- and pressure-sensitive paint measurements in short-duration hypersonic flow. *AIAA J* 39:654–659. <https://doi.org/10.2514/2.1358>
- Jiao L, Peng D, Liu Y (2018) Dynamic response of polymer ceramic pressure-sensitive paint: improved model considering thickness effect. *AIAA J* 56:2903–2906. <https://doi.org/10.2514/1.J056778>
- Jules K, Carbonaro M, Zemsch S (1995) Application of pressure sensitive paint in hypersonic flows. NASA-TM-106824
- Juliano TJ, Borg MP, Schneider SP (2015) Quiet tunnel measurements of HFiRE-5 boundary-layer transition. *AIAA J* 53:832–846. <https://doi.org/10.2514/1.J053189>
- Laurence SJ, Deiterding R, Hornung HG (2007) Proximal bodies in hypersonic flow. *J Fluid Mech* 590:209–237. <https://doi.org/10.1017/S0022112007007987>
- Laurence SJ, Hannemann K, Martinez Schramm J, Butler CS, Hannemann K (2019) Heat-flux measurements on a hypersonic inlet ramp using fast-response temperature-sensitive paint. *Exp Fluids* 60:70. <https://doi.org/10.1007/s00348-019-2711-8>
- Liu T, Sullivan JP (2005) Pressure and temperature sensitive paints. Springer, New York
- Liu T, Montefort J, Stanfield S, Palluconi S, Crafton J, Cai Z (2019) Inverse heat transfer methods for global heat flux measurements in aerothermodynamics testing. *Prog Aerosp Sci* 107:1–18. <https://doi.org/10.1016/j.paerosci.2019.04.003>
- Moelyadi MA, Breitsamter C, Laschka B (2008a) Stage-separation aerodynamics of two-stage space transport systems part 2: unsteady simulation. *J Spacecraft Rockets* 45:1240–1250. <https://doi.org/10.2514/1.35059>
- Moelyadi MA, Breitsamter C, Laschka B (2008b) Stage-separation aerodynamics of two-stage space transport systems part 1: steady-state simulations. *J Spacecraft Rockets* 45:1230–1239. <https://doi.org/10.2514/1.34828>
- Murphy KJ, Buning PG, Pamadi BN, Scallion WI, Jones KM (2004) Overview of transonic to hypersonic stage separation tool development for multi-stage-to-orbit concepts. In: 24th AIAA Aerodynamic measurement technology and ground testing conference, AIAA, pp 2004–2595
- Nettleton MA (1973) Shock attenuation in a gradual area expansion. *J Fluid Mech* 60:209–223. <https://doi.org/10.1017/S0022112073000121>
- Ozawa H, Laurence SJ, Martinez Schramm J, Wagner A, Hannemann K (2015) Fast-response temperature-sensitive-paint measurements on a hypersonic transition cone. *Exp Fluids* 56:1853. <https://doi.org/10.1007/s00348-014-1853-y>
- Peng D, Liu Y (2020) Fast pressure-sensitive paint for understanding complex flows: from regular to harsh environments. *Exp Fluids* 61:8
- Peng D, Jiao L, Sun Z, Gu Y, Liu Y (2016) Simultaneous PSP and TSP measurements of transient flow in a long-duration hypersonic tunnel. *Exp Fluids* 57(188):1–16. <https://doi.org/10.1007/s00348-016-2280-z>
- Peng D, Gu F, Li Y, Liu Y (2018) A novel sprayable fast-responding pressure-sensitive paint based on mesoporous silicone dioxide particles. *Sens Actuators A Phys* 279:390–398. <https://doi.org/10.1016/j.sna.2018.06.048>
- Risius S, Beck WH, Klein C, Henne U, Wagner A (2017) Determination of heat transfer into a wedge model in a hypersonic flow using temperature-sensitive paint. *Exp Fluids* 58:117. <https://doi.org/10.1007/s00348-017-2393-z>
- Running CL, Sakaue H, Juliano TJ (2019) Hypersonic boundary-layer separation detection with pressure-sensitive paint for a cone at

- high angle of attack. *Exp Fluids* 60:23. <https://doi.org/10.1007/s00348-018-2665-2>
- Sakaue H (2003) Anodized aluminum pressure sensitive paint for unsteady aerodynamic applications. Ph.D. dissertation, Purdue University
- Watkins AN, Buck GM, Leighty BD, Lipford WE, Oglesby DM (2009) Using pressure- and temperature-sensitive paint on the aftbody of a capsule vehicle. *AIAA J* 47:821–829. <https://doi.org/10.2514/1.37258>
- Yang L, Erdem E, Zare-Behtash H, Kontis K, Saravanan S (2012a) Pressure-sensitive paint on a truncated cone in hypersonic flow at incidences. *Int J Heat Fluid Flow* 37:9–21. <https://doi.org/10.1016/j.ijheatfluidflow.2012.05.004>
- Yang L, Zare-Behtash H, Erdem E, Kontis K (2012b) Application of AA-PSP to hypersonic flows: the double ramp model. *Sens Actuators B Chem* 161:100–107. <https://doi.org/10.1016/j.snb.2011.09.053>

Publisher's Note Springer Nature remains neutral with regard to jurisdictional claims in published maps and institutional affiliations.